

NOVEL SUPERCONDUCTOR-BASED LOW-LOSS PLASMONIC WAVEGUIDE

by

Yangyuanlong Gao

Submitted in partial fulfilment of the requirements
for the degree of Master of Applied Science

at

Dalhousie University

Halifax, Nova Scotia

August 2018

© Copyright by Yangyuanlong Gao, 2018

To my family members: my parents, my wife and my unborn baby, ChangChang

TABLE OF CONTENTS

LIST OF TABLES	v
LIST of FIGURES	vi
ABSTRACT.....	viii
LIST OF ABBREVIATIONS USED	ix
ACKNOWLEDGEMENTS	xiii
CHAPTER 1 INTRODUCTION	1
1.1 INTRODUCTION.....	1
1.2 APPLICATIONS.....	1
1.3 MOTIVATION AND OBJECTIVE	5
1.4 CONTRIBUTIONS	7
1.5 THESIS ORGANIZATION	8
CHAPTER 2 THEORETICAL BACKGROUND.....	9
2.1 INTRODUCTION.....	9
2.2 MAXWELL’S EQUATIONS AND WAVE PROPAGATION	9
2.3 BASIC PROPERTIES OF SPPs AT A SINGLE METAL-DIELECTRIC INTERFACE	12
2.4 SPPs EXCITATION METHODS	17
2.5 SUMMARY	18
CHAPTER 3 NOVEL SUPERCONDUCTOR-BASED LOW-LOSS PLASMONIC	

WAVEGUIDE	19
3.1 GEOMETRIC SHAPE OF PROPOSED ISCI-STRUCTURED WAVEGUIDE	19
3.2 MATERIAL SELECTION AND PARAMETERS DERIVATION FOR SYSTEM ANALYSIS	20
3.3 PERMITTIVITIES OF SILVER AND YBCO	23
3.4 INSULATOR-METAL-INSULATOR (IMI) WAVEGUIDE	25
3.5 FINITE ELEMENT METHOD AND GEOMETRIC MODEL	27
3.6 SIMULATION WITH DIFFERENT CORE THICKNESSES AROUND TC FREQUENCY AT 40 KELVINS.....	29
3.7 SIMULATION WITH DIFFERENT OPERATING TEMPERATURES AND PERMITTIVITY WITH FIXED CORE THICKNESS	36
3.8 SIMULATION WITH DIFFERENT MATERIAL.....	39
3.9 FIGURE OF MERIT (FoM) FOR SC-BASED AND IMI WAVEGUIDES	44
CHAPTER 4 CONCLUSION AND FUTURE WORK	49
4.1 CONCLUSIONS FROM THE RESEARCH AND DISCUSSIONS	49
4.2 FUTURE WORK	51
BIBLIOGRAPHY	52

LIST OF TABLES

Table 3.1 Real and imaginary parts of the permittivities for YBCO at 40K, 80K and Ag around TC wavelength range.....	23
Table 3.2 (a) The mode size and the propagation length at wavelength 1500 nm.....	32
Table 3.2 (b) The mode size and the propagation length at wavelength 1550 nm	33
Table 3.2 (c) The mode size and the propagation length at wavelength 1600 nm.....	34
Table 3.3 The mode size and the propagation length at fixed wavelength and core thickness at different temperature and relative permittivity	36
Table 3.4 (a) Normalized propagation length and normalized mode size of ISCI with material YBCO	40
Table 3.4 (b) Normalized propagation length and normalized mode size of ISCI with material Nb.....	41
Table 3.4 (c) Normalized propagation length and normalized mode size of IMI with material Ag.....	42
Table 3.5 (a) FoMs for YBCO -based waveguides	45
Table 3.5 (b) FoMs for Nb-based waveguides.....	46
Table 3.5 (c) FoMs for IMI waveguides	47

LIST of FIGURES

Figure 1.1 (a) The Kretschmann configuration (b) The Otto configuration.....	2
Figure 1.2 Schematic diagram of deep subwavelength plasmonic laser consisting a CdS nanowire placed on top of Ag substrate coated with a thin MgF ₂ film.....	3
Figure 1.3 Schematic diagram of nano-tweezers system with a nanogap between a silicon nanowire and substrate.....	4
Figure 1.4 Schematic diagram of cross section of hybrid terahertz plasmonic waveguide	5
Figure 2.1 Schematic view of SPPs propagating along a single metal-dielectric interface.....	13
Figure 2.2 Dispersion relation of SPP at metal/air interface.....	16
Figure 2.3 Prism coupling to excite SPPs in (a) the Kretschmann and (b) the Otto configurations	17
Figure 3.1 3D schematic diagram view of proposed ISCI structure	19
Figure 3.2 (a) Real and (b) imaginary parts of the permittivities for YBCO at 40K, 80K and Ag around TC wavelength range	24
Figure 3.3 (a) a sample prism coupler	25
Figure 3.3 (b) a sample grating coupler with taped waveguide.....	25

Figure 3.4 Schematic cross-section view of an IMI waveguide	26
Figure 3.5 2D dimensional drawing (a) outside view with mesh (not scaled) and (b) partial enlarged drawing of the center part	28
Figure 3.6 a partial enlarged drawing of the normalized energy density plot in the center part.....	30
Figure 3.7 a vertical cut line at the center (line is not scaled).....	30
Figure 3.8 1D line plot of the normalized energy density	31
Figure 3.9 (a) Normalized propagation length and (b) Normalized mode size of ISCI waveguide as a function of SC core thickness d around TC frequencies	35
Figure 3.10 Mode characteristics of ISCI waveguides as a function of temperature and ϵI at TC frequency with thickness of superconductor core of $d=110$ nm.....	38
Figure 3.11 (a) Normalized propagation length and (b) normalized mode size of ISCI (Nb and YBCO) and IMI waveguides.....	43
Figure 3.12 FoMs for SC-based (i.e. YBCO and Nb) and IMI waveguides.....	48

ABSTRACT

In this thesis, a novel plasmonic waveguide, with an insulator-superconductor (SC)-insulator (ISCI) configuration, was proposed and numerically investigated at telecommunication (TC) wavelength range. By optimizing the key parameters, the ISCI waveguide was shown to possess a superior guiding performance for the simultaneous realization of the extended propagation length (from 8600 μm to 36000 μm) and subwavelength mode confinement beyond the diffraction limit (ranging from $\lambda/4$ to $\lambda/2$). We believe the proposed waveguide shows great potential for the development of the next generation of low-loss integrated optical circuits.

LIST OF ABBREVIATIONS USED

a	A Fitting Parameter
A_g	Silver
ASM	Anti-symmetric Mode
B	Magnetic Induction or Magnetic Flux Density
b	A Fitting Parameter
c	Speed of Light
CdS	Cadmium Sulfide
D	Dielectric Displacement
d	Core Thickness
e	Unit Electron Charge
E	Electric Field
EM	Electromagnetic
FEM	Finite Element Method
FoM	Figure of Merit
E_F	Fermi Level Energy
H	Magnetic Field
HSPPs	Hybrid Surface Plasmon Polaritons
ISCI	Insulator-Superconductor-Insulator
IM ()	Imaginary Part

IMI	Insulator-Metal-Insulator
IPCs	Integrated Photonic Circuits
J	External Current Density
k_0	Wave Vector of Propagating Wave in Vacuum
k_1	Wave Vector in Material 1
k_2	Wave Vector in Material 2
K_B	The Boltzmann Constant
P	Macroscopic Polarization Field
PICs	Photonic Integrated Circuits
MgF_2	Magnesium Fluoride
L_m	Mode Size
L_{Nm}	Normalized Mode Size
L_p	Propagation Length
L_{Np}	Normalized Propagation Length
LRDLSPs	Long Range Dielectric-Loaded SPPs
MIM	Metal-Insulator-Metal
n	Refractive Index
n_{eff}	The Mode Effective Refractive Index
N	Temperature-Independent Total Density of Free Carriers
N_{se}	Superconducting Electron Density

N_{ne}	Normal Electron Density
N_b	Niobium
T	Operating Temperature
T_c	Critical Temperature
TC	Telecommunication
TM	Transverse Magnetic Modes
TE	Transverse Electric Modes
RE ()	The Real Part
SC	Superconductors
SM	Symmetrical Mode
$W(z)$	Energy Density
YBCO	Yttrium Barium Copper Oxide
ρ	External Charge Density
\hbar	Planck's Constant
β	Propagation Constant of the Traveling Waves
γ_c	The Scattering Rate at the Critical Temperature
γ	Thermal Linear Expansion Coefficient
ε	Material Permittivity
ε_0	Free Space Permittivity
ε_d	Permittivity of a Dielectric

ϵ_m	Permittivity of a Metal
ϵ_{sc}	Permittivity of a Superconductor
ϵ_∞	High Frequency Permittivity
ϵ_{Ag}	The Dielectric Constant of the Silver
m_0	Mass of a Free Electron
μ_0	Free Space Permeability
ω	Angular Frequency
ω_p	Plasma Angular Frequency
ω_e	Normal Electron Plasma Resonant Frequency
ω_{tp}	Temperature-Dependent Plasma Frequency
ω_c	Collision Frequency of Free Electrons
ω_{T_0p}	Plasma Frequency at Room Temperature
ω_{ep}	Electron–Photon Scattering Coefficient
λ	Wavelength
θ	Angle of Incident Light
1D	One Dimensional
2D	Two Dimensional
3D	Three Dimensional

ACKNOWLEDGEMENTS

I am thankful to my supervisor, Dr. Michael Cada, for his proper and timely guidance, encouragement and support throughout the entire work.

I also would like to thank the following: NSERC's (Natural Sciences and Engineering Research Council) CREATE (Collaborative Research and Training Experience) program entitled ASPIRE (Advanced Science in Photonics and Innovative Research in Engineering) of Canada and the European Regional Development Fund in the IT4Innovations National Supercomputing Center - Path to Exascale Project, project number CZ:02:1:01=0:0=0:0=16_013=0001791 within the Operational Programme Research, Development and Education.

I am also very grateful to my colleagues in ASPIRE for their selfless support. Special thanks to Dr. Youqiao Ma for many fruitful discussions and constructive advice.

I am especially grateful to my family —my parents, my wife and my unborn baby. Without my family's immense support, love and encouragement, it would have been extremely difficult for me to complete this work.

CHAPTER 1 INTRODUCTION

1.1 INTRODUCTION

Surface plasmon polaritons (SPPs) are electromagnetic waves propagating along metal–dielectric interfaces, in which surface collective excitations of free electrons in the metal are coupled to evanescent EM fields in the dielectric. The special characteristics of SPPs, such as the subwavelength mode localization beyond the diffraction limit, attract the attention of scientists and engineers from many different disciplines. Numerous research projects related to this field have been carried out and more research is underway.

1.2 APPLICATIONS

Applications such as biosensors [1], nano-lasers [2], nano-tweezers [3] and waveguides [4] are widely investigated. These applications of SPPs provide new and advanced opportunities for commercial purposes. In the following paragraphs, I offer several examples of SPPs applications.

- **Biosensors**

SPPs are used for high-sensitivity detection technologies in recent years. They are very sensitive to the dielectric perturbations at the boundary surface. The two mostly widely used methods are based on the direct coupling of light waves into SPP modes by using various configurations and

geometries to achieve a wave vector between the matching fields [5]. Commonly used geometries are the Kretschmann method and the Otto configuration, which are illustrated in Fig. 1.1. For biosensors, Kretschmann is the most common method for SPPs.

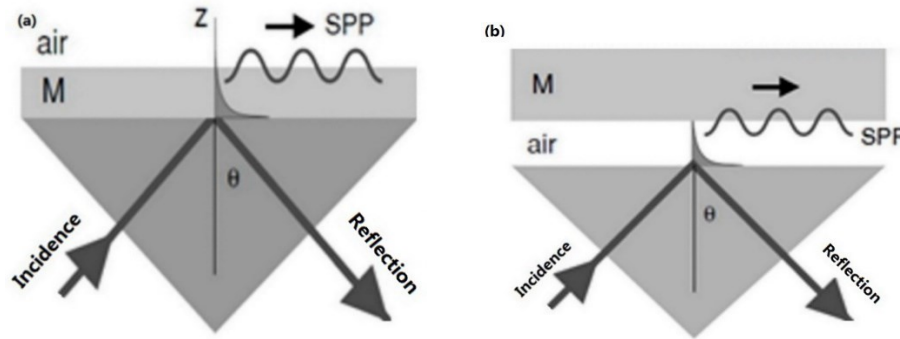


Figure 1.1 (a) The Kretschmann configuration (b) The Otto configuration

When biorecognition elements sit on the metal superstrate, the surface refractive index changes and therefore the propagation constant changes. One or more wave characteristics of the reflection light changes simultaneously, including, but not limited to, the coupling angle, coupling wavelength, phase, intensity and polarization. This variation can be detected by instruments and consequently we can receive the measurement instantly.

- Nano-lasers

SPPs allow the compact storage of optical energy in electron oscillations at the interfaces of metals and dielectrics [6-8]. Therefore, the nanolasers can be made by using a hybrid plasmonic waveguide, consisting of a high-gain cadmium sulfide (CdS) semiconductor nanowire, separated from a silver surface by a nanometer-thick insulating gap. One example is illustrated in Fig. 1.2.

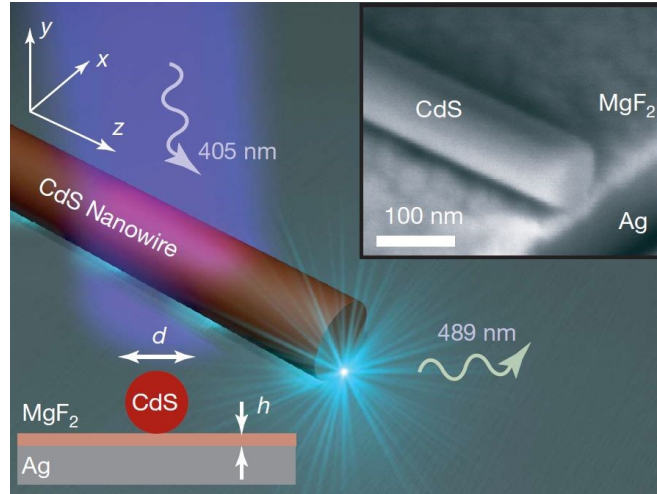


Figure 1.2 Schematic diagram of deep subwavelength plasmonic laser consisting a CdS nanowire placed on top of Ag substrate coated with a thin MgF_2 film [2]

In Fig. 1.2, the plasmonic laser consists of a CdS semiconductor nanowire on top of a silver substrate, separated by a nanometer-scale MgF_2 layer of thickness h . The coupling between the plasmonic and waveguide modes across the gap enables energy storage in nonmetallic regions. When the laser devices optically pumped 405 nm wavelength at moderate pump intensities, the wave propagation losses are compensated by gain and the cavity mode resonances take place. Therefore, there is sufficient material gain to achieve full laser oscillation and emit at the nanowire end-facets [2].

- Nano-tweezers

The hybrid SPPs system can exert the optical force on a dielectric waveguide by a metallic substrate. The coupled waveguide system consists of a dielectric cylinder waveguide and a metallic substrate with a nanoscale gap in between, which is illustrated in Fig. 1.3. This

configuration leads to deep subwavelength optical energy confinement with ultralow mode propagation loss and results in the enhanced optical forces at low input optical power.

Furthermore, the hybridization between the surface plasmon modes and waveguide modes allows efficient optical trapping of single dielectric nanoparticle with a size of only several nanometers in the gap region, manifesting various opto-mechanical applications such as nanoscale optical tweezers [9].

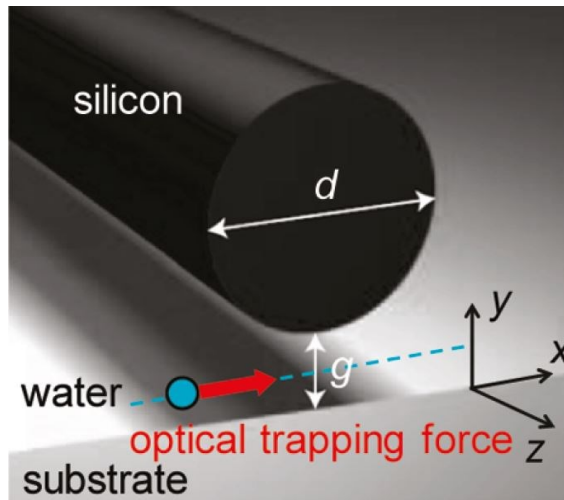


Figure 1.3 Schematic diagram of nano-tweezers system with a nanogap between a silicon nanowire and substrate [9]

- SPPs waveguides

Various types of plasmonic waveguides have been proposed recently, including, but not limited to, the metal films, metal grooves, metal strips, metal wedges, hybrid Bragg and hybrid plasmonic waveguides. Those waveguides can confine electromagnetic energy firmly near the interface, beyond the diffraction limit of a transmission wave. However, the problem of inherent losses must still be solved. Further investigation is needed to develop the next generation of photonic

integrated circuits (PICs). One of the proposals is a hybrid terahertz plasmonic waveguide, which is illustrated in Fig. 1.4.

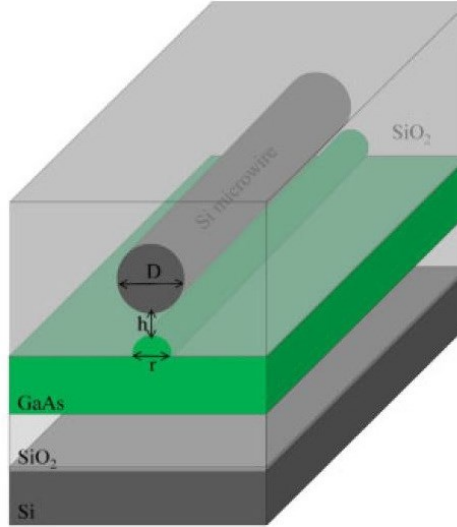


Figure 1.4 Schematic diagram of cross section of hybrid terahertz plasmonic waveguide [10]

This waveguide has a unique ridge. The new structure has a better performance than the other conventional hybrid SPPs (HSPPs) waveguide. The structure with the same propagation length has a much higher mode confinement with a one order of magnitude smaller normalized mode area [10].

1.3 MOTIVATION AND OBJECTIVE

Although the technique of SPPs are widely used in the real electronic and photonic applications, one of the main drawbacks is the large propagation loss associated with the inherent metal properties. Many methods to solve this problem have been proposed, such as HSPPs waveguides [4], long range dielectric-loaded SPPs (LRDLSPs) waveguides [11], hybrid semiconductor

waveguide and so on [10]. There are still gaps between the theoretical improvement in experiments and real environment applications. Some reasons for this are listed as follows:

1. The propagation length of SPPs are very short in metals and semiconductors materials due to the large dissipative losses. For example, even if the silver exhibits a lowest dissipative loss in TC wavelengths, the propagation length of the silver is as short as 1200 μm [12]. Additionally, such losses will further increase if the mode size is downscaled to a subwavelength level.
2. The complexity of the new geometrical structure could cause some problems. For instance, although the propagation length of up to 2mm for the hybridized SPP (HSPP) waveguides mode has recently been reported, it suffers from a complicated fabrication process [13]. Many of the SPPs waveguide structures are within the nanometer scale. The size of the structure will never be exactly as we designed; even if the variation is within the acceptable tolerance, the performance of the SPPs devices could be affected.
3. The usage of the gain medium could mitigate the propagation loss, but it is found that even the best gain materials available are barely enough to compensate for the metallic loss [15].

To minimize the influencing factors mentioned above, the Metal-Insulator-Metal (MIM) configuration is proposed. This configuration has a relatively easy manufacturing structure and is not as influenced by the doping concentration as are semiconductors. However, the MIM configuration still must overcome the inherent losses caused by using metal materials. One interesting approach is to focus on changing the properties of the plasmonic materials, by selecting an appropriate material with relative low losses, i.e. highly doped semiconductors, superconductors (SCs) and graphenes [14]. One spontaneous idea is to replace the metal layer into highly doped semiconductors, SC or graphenes. Research related to that idea has been conducted; for example, in Ref. 10, the authors concluded that the proposed SC-based plasmonic waveguide can provide a significant small mode size. Furthermore, this structure can be easily integrated with and/or embedded into other photonic components. However, the losses still aren't negligible at TC range due to the eliminated conductivity. It is intuitive to consider a reversed construction; i.e., to build the middle layer with the superconductor and attach dielectric layers on both of its sides, which is known as long-range plasmonic waveguides [15]. The objective in this paper is to find out the properties of SPPs based on this ISCI structure, especially focusing on the propagation length and mode size.

1.4 CONTRIBUTIONS

I proposed a novel plasmonic waveguide with an ISCI configuration. In this thesis, my focus is on yttrium barium copper oxide (YBCO) as the SC material. By using COMSOL Multiphysics simulation software, this waveguide with YBCO core has been numerically studied at TC

frequency range. Furthermore, by optimizing the key parameters, namely the working frequency, the core thickness, the cladding permittivity and the working temperature, as well as comparing it with a different core material, i.e. the A_g core and the conventional SC N_b core with the same structure, I showed that this ISCI waveguide, using YBCO as the core material, offers a superior guiding performance. An extended propagation length (from 8600 μm to 36000 μm) and a subwavelength mode confinement beyond the diffraction limit (ranging from $\lambda/4$ to $\lambda/2$) were achieved.

1.5 THESIS ORGANIZATION

The thesis is organized as follows. Chapter 2 presents an overview of the fundamental theories of SPPs, including the physical and mathematical explanations to wave propagation and SPPs. As well, the properties of SPPs and the derivation of SPPs dispersion relation use Maxwell equations on a metal/dielectric interface. At the end of Chapter 2, two brief SPPs excitation methods have been reviewed. In Chapter 3, an ISCI configuration is proposed. I start with the geometric shape of this proposed waveguide, followed by material selection and parameters derivation for system analysis. The selected material ensured the excitation of the SPPs modes. Two key parameters, the mode size and the propagation length, are introduced and calculated in the mode analysis for ISCI waveguides by using COMSOL Multiphysics simulation software. After analyzing the data, I confirmed that this ISCI waveguide using YBCO as the core material holds a better guiding performance than the other two core materials. In Chapter 4, I conclude the thesis, and discuss possible improvements and suggestions for future work.

CHAPTER 2 THEORETICAL BACKGROUND

2.1 INTRODUCTION

As stated at the beginning of Chapter 1, SPPs are electromagnetic waves coupled to collective electron oscillations and propagating along the interface between metal and dielectric media, and exponentially decaying into both neighboring media. Since SPPs are electromagnetic waves, it is important to start with Maxwell's equations and wave propagation.

2.2 MAXWELL'S EQUATIONS AND WAVE PROPAGATION

The well-known Maxwell's equations of macroscopic electromagnetism have the following form:

$$\nabla \cdot \mathbf{D} = \rho \quad (2.1a)$$

$$\nabla \cdot \mathbf{B} = 0 \quad (2.1b)$$

$$\nabla \times \mathbf{E} = -\frac{\partial \mathbf{B}}{\partial t} \quad (2.1c)$$

$$\nabla \times \mathbf{H} = \mathbf{j} + \frac{\partial \mathbf{D}}{\partial t} \quad (2.1d)$$

Where \mathbf{D} , \mathbf{B} , \mathbf{E} and \mathbf{H} are representing the dielectric displacement, the magnetic flux density, the electric field and the magnetic field, respectively. The external or driving volume charge and current density, ρ and \mathbf{j} , give rise to the electromagnetic fields obeying the Maxwell equations as well. In this thesis, we assumed that all material media are linear, isotropic, homogenous and nonmagnetic, which is true for almost all natural media at optical frequencies. Therefore, the magnetic constitutive relation in free space can be written as:

$$\mathbf{B} = \mu_0 \mathbf{H} \quad (2.2a)$$

Where μ_0 is the permeability of free space. Similarly, the general electric constitutive relation in free space can be written as:

$$\mathbf{D} = \epsilon_0 \mathbf{E} + \mathbf{P} \quad (2.2b)$$

Where ϵ_0 is the free space permittivity and \mathbf{P} is a macroscopic polarization field, which is a function of the applied electrical field.

In the absence of external charges and current ρ and \mathbf{j} , Maxwell's equation becomes:

$$\nabla \cdot \mathbf{E} = 0 \quad (2.3a)$$

$$\nabla \cdot \mathbf{H} = 0 \quad (2.3b)$$

$$\nabla \times \mathbf{E} = -\frac{\partial \mathbf{B}}{\partial t} \quad (2.3c)$$

$$\nabla \times \mathbf{H} = \frac{\partial \mathbf{D}}{\partial t} \quad (2.3d)$$

Taking the curl operation of both sides of equation 2.3c, we have:

$$\nabla \times \nabla \times \mathbf{E} = -\mu_0 \frac{\partial(\nabla \times \mathbf{H})}{\partial t} \quad (2.4)$$

Combining equation 2.3d, the equation 2.4 can be written as:

$$\nabla \times \nabla \times \mathbf{E} = -\mu_0 \frac{\partial^2 \mathbf{D}}{\partial t^2} \quad (2.5)$$

Applying the vector identity, $\nabla \times \nabla \times \mathbf{E} = \nabla(\nabla \cdot \mathbf{E}) - \nabla^2 \mathbf{E}$, equation 2.5 can be written as:

$$\nabla(\nabla \cdot \mathbf{E}) - \nabla^2 \mathbf{E} = -\mu_0 \epsilon_0 \frac{\partial^2 \mathbf{E}}{\partial t^2} \quad (2.6)$$

Applying equation 2.3a, then equation 2.6 can be rewritten as:

$$\nabla^2 \mathbf{E} - \mu_0 \epsilon_0 \frac{\partial^2 \mathbf{E}}{\partial t^2} = 0 \quad (2.7)$$

Assuming a time-harmonic dependence for the electromagnetic field $\mathbf{E}(\mathbf{r}, t) = \mathbf{E}(\mathbf{r})e^{-i\omega t}$, then

$$\frac{\partial^2 \mathbf{E}}{\partial t^2} = -\omega^2 \mathbf{E}(\mathbf{r})e^{-i\omega t} \quad (2.8)$$

Therefore, equation 2.7 can be written as:

$$\nabla^2 \mathbf{E} + \mu_0 \varepsilon_0 \omega^2 \mathbf{E} = 0 \quad (2.9)$$

The free space permittivity ε_0 defined as:

$$\varepsilon_0 = \frac{1}{\mu_0 c^2} \quad (2.10)$$

Where c is the defined value for the speed of light in classical vacuum in SI units.

Therefore, equation 2.9 can be written as:

$$\nabla^2 \mathbf{E} + \left(\frac{\omega}{c}\right)^2 \mathbf{E} = 0 \quad (2.11)$$

Since the wave vector of the propagating wave in vacuum k_0 is defined as:

$$k_0 = \frac{\omega}{c} \quad (2.12)$$

Where c is the speed of light in a vacuum.

Therefore, we finally arrive at the Helmholtz equation from equation 2.11:

$$\nabla^2 \mathbf{E} + k_0^2 \mathbf{E} = 0 \quad (2.13)$$

Previously, we considered the electromagnetic (EM) waves that propagate in free space, assuming

the EM wave propagates along the x -direction in a Cartesian coordinate system. The permittivity

ε depends only on one spatial coordinate, saying $\varepsilon = \varepsilon(z)$. From Maxwell's equations, the

wave equations can be rewritten as:

$$\frac{\partial^2 \mathbf{E}(z)}{\partial z^2} + (k_0 \varepsilon - \beta^2) \mathbf{E} = 0 \quad (2.14a)$$

$$\frac{\partial^2 \mathbf{H}(z)}{\partial z^2} + (k_0 \varepsilon - \beta^2) \mathbf{H} = 0 \quad (2.14b)$$

Where β is the propagation constant of the traveling waves and corresponds to the component of

the wave vector in the direction of propagation.

For a time-harmonic dependence ($\frac{\partial}{\partial t} = -i\omega$) of the EM field, the following set of coupled equations can be arrived at:

$$\frac{\partial E_z}{\partial y} - \frac{\partial E_y}{\partial z} = i\omega\mu_0 H_x \quad (2.15a)$$

$$\frac{\partial E_x}{\partial z} - \frac{\partial E_z}{\partial x} = i\omega\mu_0 H_y \quad (2.15b)$$

$$\frac{\partial E_y}{\partial x} - \frac{\partial E_x}{\partial y} = i\omega\mu_0 H_z \quad (2.15c)$$

$$\frac{\partial H_z}{\partial y} - \frac{\partial H_y}{\partial z} = -i\omega\epsilon_0 \epsilon E_x \quad (2.15d)$$

$$\frac{\partial H_x}{\partial z} - \frac{\partial H_z}{\partial x} = -i\omega\epsilon_0 \epsilon E_y \quad (2.15e)$$

$$\frac{\partial H_y}{\partial x} - \frac{\partial H_x}{\partial y} = -i\omega\epsilon_0 \epsilon E_z \quad (2.15f)$$

2.3 BASIC PROPERTIES OF SPPs AT A SINGLE METAL-DIELECTRIC INTERFACE

The simplest geometric supporting SPPs is a single, flat interface plane with two different media, which is shown in Fig. 2.1. When $z < 0$, the complex dielectric constant (ϵ_m) of a metal is negative. When $z > 0$, the complex dielectric constant (ϵ_d) of a dielectric is positive. Assuming that the SPPs wave propagates along the x-direction with a propagation constant β , then $\frac{\partial}{\partial x} = -i\beta$. Since the structure is a purely 2-dimensional structure, there is no spatial variation along the y-direction ($\frac{\partial}{\partial y} = 0$); therefore, the set of equation 2.15 can be simplified as:

$$\frac{\partial E_y}{\partial z} = -i\omega\mu_0 H_x \quad (2.16a)$$

$$\frac{\partial E_x}{\partial z} - i\beta E_z = i\omega\mu_0 H_y \quad (2.16b)$$

$$i\beta E_y = i\omega\mu_0 H_z \quad (2.16c)$$

$$\frac{\partial H_y}{\partial z} = i\omega\epsilon_0\epsilon E_x \quad (2.16d)$$

$$\frac{\partial H_x}{\partial z} - i\beta H_z = -i\omega\epsilon_0\epsilon E_y \quad (2.16e)$$

$$i\beta H_y = -i\omega\epsilon_0\epsilon E_z \quad (2.16f)$$

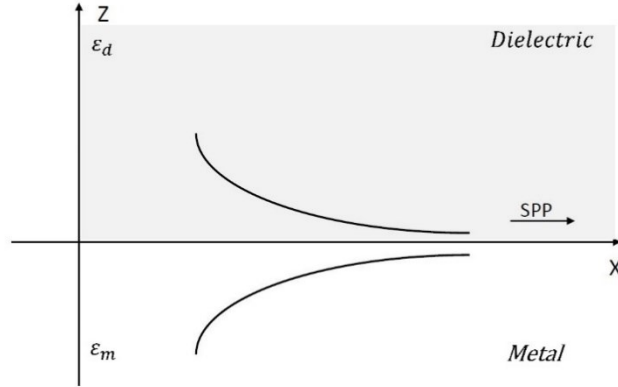


Figure 2.1 Schematic view of SPPs propagating along a single metal-dielectric interface

There exist two sets of self-consistent solutions for equation 2.16, namely the transverse magnetic (TM) modes and the transverse electric (TE) modes. The former only has the field components E_x , E_z and nonzero H_y and the latter only has the field components H_x , H_z and nonzero E_y .

For TM mode, equation 2.16 is reduced to:

$$\frac{\partial E_x}{\partial z} - i\beta E_z = i\omega\mu_0 H_y \quad (2.17a)$$

$$E_x = -\frac{i}{\omega\epsilon_0\epsilon} \frac{\partial H_y}{\partial z} \quad (2.17b)$$

$$E_z = -\frac{\beta}{\omega\epsilon_0\epsilon} H_y \quad (2.17c)$$

The SPPs dispersion relation for TM mode can be derived from equation 2.16 in upper and lower space as follows:

For $z < 0$

$$H_y(z) = A_1 e^{i\beta x} e^{k_1 z} \quad (2.18a)$$

$$E_x(z) = -\frac{iA_1 k_1}{\omega \epsilon_0 \epsilon_m} e^{i\beta x} e^{k_1 z} \quad (2.18b)$$

$$E_z(z) = -\frac{A_1 \beta}{\omega \epsilon_0 \epsilon_m} e^{i\beta x} e^{k_1 z} \quad (2.18c)$$

And for $z > 0$

$$H_y(z) = A_2 e^{i\beta x} e^{-k_2 z} \quad (2.19a)$$

$$E_x(z) = \frac{iA_2 k_2}{\omega \epsilon_0 \epsilon_d} e^{i\beta x} e^{-k_2 z} \quad (2.19b)$$

$$E_z(z) = -\frac{A_2 \beta}{\omega \epsilon_0 \epsilon_d} e^{i\beta x} e^{-k_2 z} \quad (2.19c)$$

$$\text{Where } k_i^2 + k_0^2 \epsilon_i = \beta^2 \quad (2.20)$$

($k_i = k_1, k_2$, and $\epsilon_i = \epsilon_m$ for $z < 0$, otherwise $\epsilon_i = \epsilon_d$)

Applying continuity and boundary conditions at $z=0$, we have:

$$A_1 = A_2 \quad \text{and} \quad \frac{k_1}{k_2} = -\frac{\epsilon_m}{\epsilon_d} \quad (2.21)$$

$\text{Re}[k_1]$ and $\text{Re}[k_2]$ must be positive since the SPPs field is confined to the interface and evanescently decays in the z -direction; i.e., $E_z(z)$ should be exponential decay in both equation 2.18c and equation 2.19c. That also means the real part of the dielectric permittivities $\text{Re}[\epsilon_m] < 0$ if $\text{Re}[\epsilon_d] > 0$. It is known that this condition is satisfied in the visible and infrared wavelength range [16]. Due to this, the SPPs can exist for TM polarization. If we combine equation 2.20 and equation 2.21, the dispersion relation of SPPs in a single metal-dielectric interface can be derived as:

$$\beta = k_0 \sqrt{\frac{\epsilon_m \epsilon_d}{\epsilon_m + \epsilon_d}} \quad (2.22)$$

For TE mode, equation 2.16 is reduced to:

$$\frac{\partial H_x}{\partial z} - i\beta H_z = -i\omega \epsilon_0 \epsilon E_y \quad (2.23a)$$

$$\frac{\partial E_y}{\partial z} = -i\omega \mu_0 H_x \quad (2.23b)$$

$$i\beta E_y = i\omega \mu_0 H_z \quad (2.23c)$$

The SPPs dispersion relation for TE mode can be derived from equation 2.16 in upper and lower space as follows:

For $z < 0$

$$E_y(z) = A_3 e^{i\beta x} e^{k_1 z} \quad (2.24a)$$

$$H_x(z) = \frac{iA_3 k_1}{\omega \mu_0} e^{i\beta x} e^{k_1 z} \quad (2.24b)$$

$$H_z(z) = \frac{A_3 \beta}{\omega \mu_0} e^{i\beta x} e^{k_1 z} \quad (2.24c)$$

And for $z > 0$

$$E_y(z) = A_4 e^{i\beta x} e^{-k_2 z} \quad (2.25a)$$

$$H_x(z) = -\frac{iA_4 k_2}{\omega \mu_0} e^{i\beta x} e^{-k_2 z} \quad (2.25b)$$

$$H_z(z) = \frac{A_4 \beta}{\omega \mu_0} e^{i\beta x} e^{-k_2 z} \quad (2.25c)$$

$$\text{Where } k_i^2 + k_0^2 \epsilon_i = \beta^2 \quad (2.26)$$

($k_i = k_1, k_2$, and $\epsilon_i = \epsilon_m$ for $z < 0$, otherwise $\epsilon_i = \epsilon_d$)

Applying continuity and boundary conditions at $z=0$, we have:

$$A_3 = A_4 \quad \text{and} \quad k_1 = -k_2 \quad (2.27)$$

Equation 2.27 does not satisfy the confinement to the surface requirement; namely that $\text{Re}[k_1]$ and $\text{Re}[k_2]$ must be all positive. Therefore, SPPs cannot exist in TE mode.

We can examine the properties of SPPs by considering the dispersion relation expressed by equation 2.22. Fig. 2.2 shows the dispersion relation of SPPs for an air/metal interface.

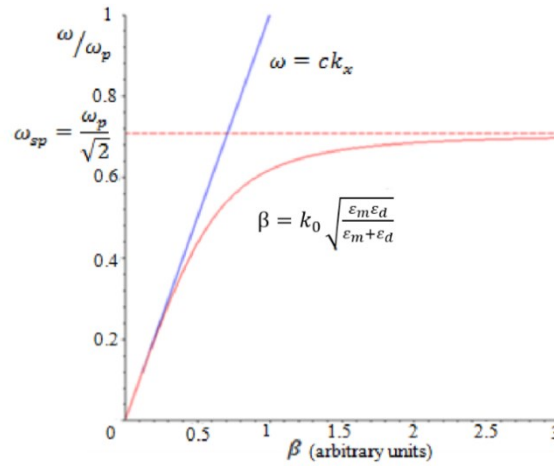


Figure 2.2 Dispersion relation of SPP at metal/air interface [17]

The complex frequency dependent permittivity of metal is characterized by the Drude model [18]

$$\epsilon_m(\omega) = \epsilon_\infty - \frac{\omega_p^2}{\omega(\omega + i\gamma)} \quad (2.28)$$

Where ϵ_∞ is the high frequency permittivity, γ is the damping term and ω_p is the plasma angular frequency. It is easy to see that the SPPs plot stays on the right side of the plot of the light in air. That means the wave vector of SPPs is always larger than that of the light in free space at the given frequency. Under this condition, the SPPs cannot form due to this wave vector mismatch. Therefore, wave vector matching methods need to be implemented. Two methods will be discussed in section 2.4.

2.4 SPPs EXCITATION METHODS

In order to couple light into SPPs mode, two prism-based methods have been widely used, namely, the Kretschmann configuration and the Otto configuration [19], which are shown in Fig. 2.3(a) and 2.3(b)

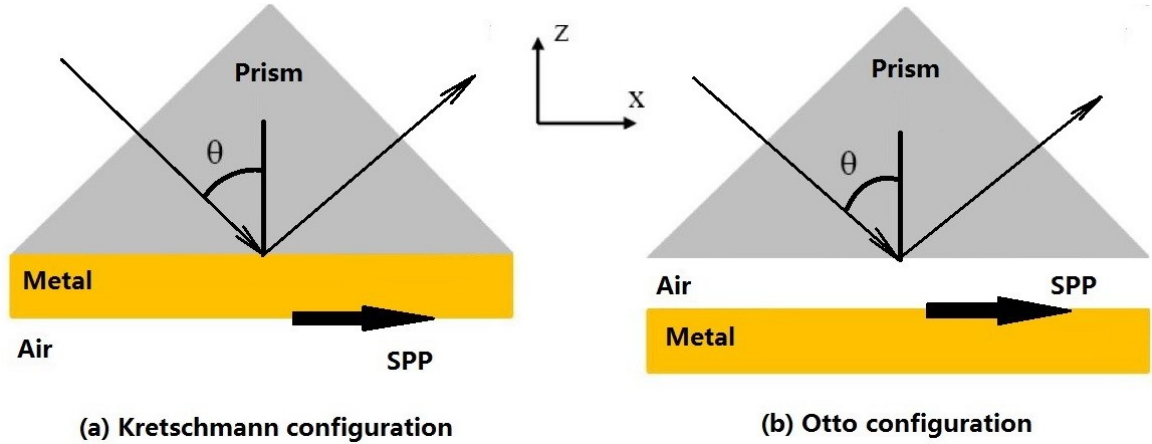


Figure 2.3 Prism coupling to excite SPPs in (a) the Kretschmann and (b) the Otto configurations [19]

For the Kretschmann configuration, shown in Fig. 2.3a, a thin metal film is deposited on the bottom surface of a glass prism with a dielectric constant ϵ . When the attenuated total reflection [20] takes place at the interface between prism and metal, the evanescent wave extends outside the prism [20]. This wave has an in-plane momentum $k_x = k\sqrt{\epsilon}\sin\theta$, where θ is the incident angle from the prism to air and is much larger than the critical angle. It is possible that the in-plane momentum is larger than the momentum in air. Therefore, the SPPs at the metal-air interface can be excited under this configuration.

For the other geometry configuration, namely the Otto configuration, the glass prism is separated from the metal field by a thin air gap. Similar to the Kretschmann configuration, when the attenuated total reflection [20] takes place at the interface between prism and air, the evanescent wave can be coupled to the SPPs at the metal-air interface.

2.5 SUMMARY

In this chapter, the theoretical background of SPPs was discussed. More particularly, in section 2.2, the Maxwell's equation and wave propagation were discussed. In section 2.3, the basic properties of SPPs and the dispersion relation at a single metal-dielectric interface were presented. The SPPs excitation methods were introduced in general in section 2.4.

CHAPTER 3 NOVEL SUPERCONDUCTOR-BASED LOW-LOSS PLASMONIC WAVEGUIDE

3.1 GEOMETRIC SHAPE OF PROPOSED ISCI-STRUCTURED WAVEGUIDE

The proposed waveguide contains a superconductor core sandwiched between two identical semi-infinite insulator claddings. The thickness of the core is noted as d . In addition, the permittivity of the core and claddings are represented by ϵ_{sc} and ϵ_I respectively. The coordinate system is also depicted in Fig. 3.1. The following discussion will only consider the TC frequency rather than terahertz (THz) frequency, which rises from the fact that the SPPs mode is loosely localized in the vicinity of the conductor's surface at THz range [21].

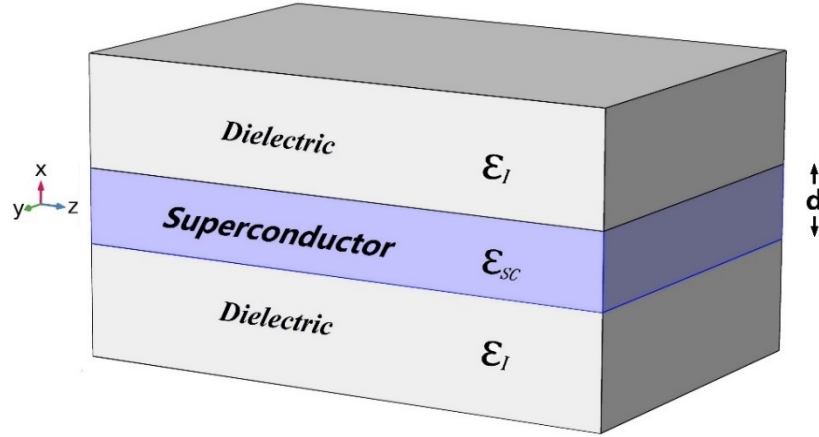


Figure 3.1 3D schematic diagram view of proposed ISCI structure

3.2 MATERIAL SELECTION AND PARAMETERS DERIVATION FOR SYSTEM ANALYSIS

As discussed at the end of section 1.2, I choose SC materials due to the non-lossy capacity. In this thesis, a high-temperature superconductor, YBCO, has been chosen to evaluate the plasmonic waveguiding performance. This is the first material yet discovered to become superconducting above the boiling point of liquid nitrogen (77 K) at about 90 K. It should be mentioned that the Cooper pair can be broken under light illumination with a certain photon energy above the superconducting band gap by applying the Bardeen-Cooper-Schrieffer (BCS) theory [22]. Therefore, the superconducting phenomenon disappears at TC frequency (or in other words, it is strictly SC-like material). However, the guiding performance of SC-based plasmonic waveguide is still superior to normal metal material. For simplicity, I will use SC rather than SC-like material in the rest of this thesis.

It is assumed that the SPPs wave propagates along the z-direction with a propagation constant of β and there are no spatial variations along the y direction (see Fig. 3.1). Thus, the magnetic fields H_y can be expressed as:

$$H_y(x) = Ae^{i\beta z - (x-d/2)\sqrt{\beta^2 - k_0^2 \epsilon_l}} \quad (x > d/2) \quad (3.1a)$$

$$H_y(x) = Be^{i\beta z - (x+d/2)\sqrt{\beta^2 - k_0^2 \epsilon_l}} \quad (x < -d/2) \quad (3.1b)$$

$$H_y(x) = Ce^{i\beta z - (x-d/2)\sqrt{\beta^2 - k_0^2 \epsilon_{sc}}} + De^{i\beta z - (x+d/2)\sqrt{\beta^2 - k_0^2 \epsilon_{sc}}} \quad (-d/2 < x < d/2) \quad (3.1c)$$

where the electric fields, $E_z(x)$ and $E_x(x)$, are given by:

$$E_z(x) = -\frac{i}{\omega \epsilon_0 \epsilon_i} \frac{\partial H_y}{\partial z} \quad (3.2a)$$

$$E_x(x) = -\frac{\beta}{\omega \epsilon_0 \epsilon_i} H_y \quad (3.2b)$$

where $\epsilon_i = \epsilon_{sc}$ for $-d/2 < x < d/2$ otherwise $\epsilon_i = \epsilon_l$.

According to BCS theory and the two-fluid model reported in Ref. 21, the permittivity of YBCO under the critical temperature at TC frequency can be described by the Drude model:

$$\epsilon_{sc} = \frac{\omega^2 - \omega_p^2}{\omega^2(\omega^2 \tau^2 + 1)} + \frac{\tau^2(\omega^2 - \omega_p^2 - \omega_e^2)}{\omega^2 \tau^2 + 1} + i \frac{\omega_e^2 \tau}{\omega^3 \tau^2 + \omega} \quad (3.3)$$

where τ is the relaxation time, ω , ω_p and ω_e represent the angular frequency, plasma frequency and normal electron plasma resonant frequency respectively, which can be expressed as:

$$\tau = \frac{\left(\frac{T}{T_c}\right)^a - b \left(\frac{T}{T_c}\right)^{(a+1)} + b \left(\frac{T}{T_c}\right)}{\left(\frac{T}{T_c}\right)^{(a+1) \gamma_c}} \quad (3.4)$$

$$\omega_p = e \sqrt{\frac{N_{se}}{m_0 \epsilon_0}} \quad (3.5)$$

$$\omega_e = e \sqrt{\frac{N_{ne}}{m_0 \epsilon_0}} \quad (3.6)$$

where a and b are the fitting parameters, e is the unit electron charge, m_0 is the mass of a free electron, N is the temperature-independent total density of free carriers, T_c and T are the critical and operating temperatures, respectively, γ_c is the scattering rate at T_c , $N_{se} = N[1 - (T_c/T)^4]$ and $N_{ne} = N(T_c/T)^4$ are the superconducting electron and normal electron densities respectively.

To have a reasonable comparison, well-known silver (Ag) was chosen as the metal material due to its relative low loss. The dielectric constant of Ag can be expressed as:

$$\epsilon_{Ag} = \epsilon_{\infty} - \frac{\omega_{tp}^2}{\omega(\omega + i\omega_c)} \quad (3.7)$$

where ω_{tp} is the temperature-dependent plasma frequency and ω_c is the collision frequency of free electrons. They can be written as:

$$\omega_{tp} = \frac{\omega_{T0p}}{\sqrt{1 + 3\gamma(T - T_0)}} \quad (3.8)$$

$$\omega_c = \frac{\Lambda}{\hbar} + \frac{0.012\pi^4[(TK_B)^2 + (\frac{\hbar\omega}{2\pi})^2]}{\hbar E_F} \quad (3.9)$$

where ω_{T0p} , γ and \hbar are the plasma frequency at room temperature T_0 , the thermal linear expansion coefficient and the Planck's constant respectively, $\Lambda = \hbar\omega_{ep}$, where ω_{ep} is the electron-photon scattering coefficient, E_F is the Fermi level energy, and K_B is the Boltzmann constant.

The parameters of the Drude model used for Ag are as follows: $\epsilon_{\infty} = 3.67$, $\gamma = 1.5 \times 10^{-15}$, $E_F = 2980 \text{ TH}_z$, $\omega_{T0p} = 1.38 \times 10^{16} \text{ Hz}$ and $\Lambda = 4 \text{ TH}_z$ [23], while the parameters for YBCO under the critical temperature are: $T_c = 88 \text{ K}$, $a = 1.5$, $b = 10$, $N = 1.255 \times 10^{27} \text{ m}^{-3}$, $\gamma_c = 0.28 \times 10^{14} \text{ Hz}$ [24].

3.3 PERMITTIVITIES OF SILVER AND YBCO

In section 3.2, the closed-form expression of the permittivity for both Ag and YBCO has been derived. Now I can analyze the material properties of YBCO and Ag at different temperatures. The real and the imaginary parts of the complex permittivity around TC frequency for Ag and YBCO at different temperatures is shown in Table 3.1.

Table 3.1 Real and imaginary parts of the permittivities for YBCO at 40K, 80K and Ag around TC wavelength range

Wavelength	40K YBCO Permittivity		80K YBCO Permittivity		40K Ag Permittivity	
(nm)	Real	Imaginary	Real	Imaginary	Real	Imaginary
1500	-1.52580	9.68590E-05	-1.52570	0.01459300	-117.01000	2.624100
1510	-1.55960	9.88090E-05	-1.55950	0.01488600	-118.62000	2.677000
1520	-1.59370	1.00790E-04	-1.59350	0.01518400	-120.25000	2.730500
1530	-1.62790	1.02790E-04	-1.62780	0.01548600	-121.88000	2.784700
1540	-1.66240	1.04820E-04	-1.66220	0.01579100	-123.53000	2.839700
1550	-1.69700	1.06870E-04	-1.69690	0.01610100	-125.18000	2.895300
1560	-1.73200	1.08950E-04	-1.73180	0.01641500	-126.85000	2.951700
1570	-1.76710	1.11060E-04	-1.76690	0.01673200	-128.53000	3.008800
1580	-1.80250	1.13200E-04	-1.80230	0.01705400	-130.22000	3.066600
1590	-1.83800	1.15360E-04	-1.83790	0.01738000	-131.92000	3.125200
1600	-1.87390	1.17550E-04	-1.87370	0.01771000	-133.63000	3.184500

The real and imaginary parts vs. wavelength around TC frequency range for both Ag and YBCO is shown in Fig. 3.2(a) and (b). Notice that all the real parts of the permittivities for Ag and YBCO are negative, which provides the essential requirement to excite the SPPs modes.

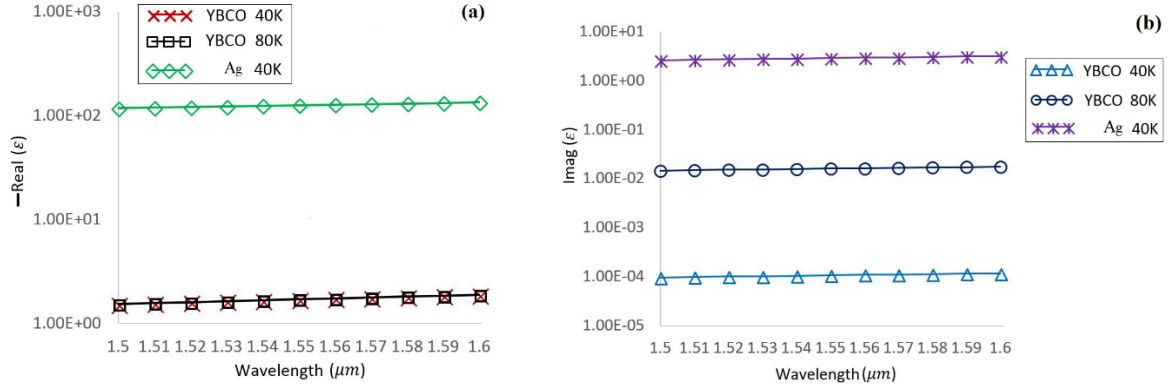


Figure 3.2 (a) Real and (b) imaginary parts of the permittivities for YBCO at 40K, 80K and Ag around TC wavelength range

Fig. 3.2 (b) clearly shows that the YBCO at 40K has lower absorption than the case operating at 80K from 1500 nm to 1600 nm, while the Ag almost has a constant absorption and a higher imaginary part than that of YBCO, indicating that the absorption of Ag is much higher than YBCO when YBCO is under the critical temperature. On the other hand, it is found that the dispersions for YBCO are almost the same at 40K and 80K; thus it is hard to distinguish those two representative lines, as shown in Fig. 3.2 (a). However, the absorption for YBCO at 80K is much higher than that at 40K, i.e. the loss is higher at 80K (which is close to the critical temperature). Even so, the absorption of YBCO is much less than that of Ag when it is below the critical temperature.

3.4 INSULATOR-METAL-INSULATOR (IMI) WAVEGUIDE

To analyze IMI waveguides, we need to couple a light beam into the waveguide. The two most common elements, the prism coupler and the grating coupler, are widely used for experiments. Those two elements are shown in Fig. 3.3(a) and Fig. 3.3(b).

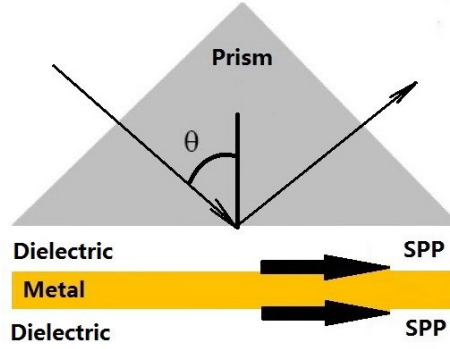


Figure 3.3(a) a sample prism coupler

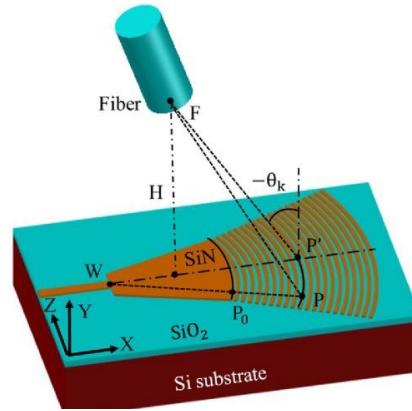


Figure 3.3(b) a sample grating coupler with tapered waveguide [25]

Once the light beam is coupled with an IMI or an ISCI waveguide, the interaction between the SPPs at the two metal surfaces gives rise to the coupled mode, namely, the symmetrical mode (SM) and the anti-symmetrical mode (ASM). When the thickness of the central layer decreases, the confinement of the ASM close to the metal surface

increases. The propagation length is reduced. In contrast to the ASM, when the thickness of the central layer decreases, the confinement of the SM close to the metal surface decreases, the field spreads deeply into the dielectric layer. Therefore, the propagation length increases exceedingly. Therefore, the SM for the IMI configuration attracts significant interest from researchers. It is also one of the initial points of interest of this thesis.

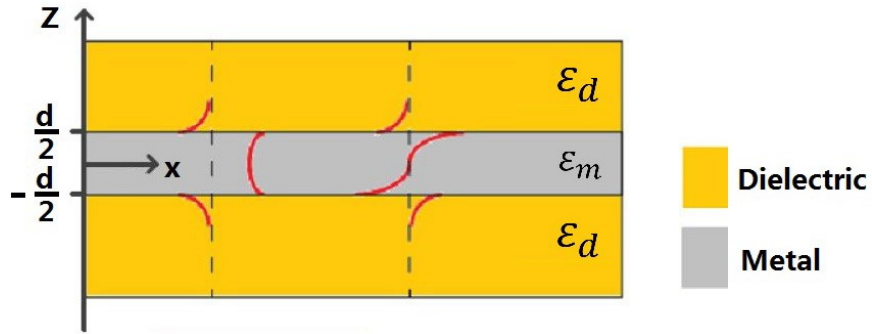


Figure 3.4 Schematic cross-section view of an IMI waveguide. (The red lines denote $\text{Re}(E_z)$)

Previous studies of plasmonic waveguides confirmed that they could not only surpass the diffraction limit but also possess relative long propagation lengths. Therefore, the quantity evaluation of SPPs waveguides mode characteristics are mainly based on two critical parameters, which are the mode size (L_m) and propagation length (L_p). Therefore, the evaluation of those two characteristic properties could deliver an objective assessment of the proposed ISCI waveguide structure. The propagation length (L_p) and mode size (L_m) are defined as:

$$L_p = \frac{\lambda}{4\pi \text{Im}(n_{\text{eff}})} \quad (3.10)$$

$$L_m = \frac{\int W(z)dz}{\max\{W(z)\}} \quad (3.11)$$

Where λ is the operating wavelength, $\text{IM}(n_{\text{eff}})$ is the imaginary part of the mode effective refractive index n_{eff} and $W(z)$ is the energy density.

The energy density $W(z)$ defined as:

$$W(z) = \frac{1}{2} \text{Re} \left\{ \frac{d[\omega \varepsilon(z)]}{d\omega} \right\} |E(z)|^2 + \frac{1}{2} \mu_0 |H(z)|^2 \quad (3.12)$$

Where $E(z)$ and $H(z)$ are the electric and magnetic fields correspondingly.

In order to have a visualized examination, those two parameters are normalized and defined as

$L_{Nm} = \frac{L_m}{L_0}$ and $L_{Np} = \frac{L_p}{\lambda}$, respectively, where L_0 is defined as $L_0 = \frac{\lambda}{2}$. It is important to point out that the value of L_m must be less than that of L_0 to overcome the diffraction limit.

3.5 FINITE ELEMENT METHOD AND GEOMETRIC MODEL

The finite element method (FEM) is a numerical method for solving problems in engineering and mathematical physics, which can be used to approximate the solution to boundary value problems for various partial differential equations. By using variational methods from the calculus of variations to approximate solutions by minimizing an associated error function, the analytical solution can be solved using the computational method. A commercial software program, COMSOL Multiphysics, is utilized in this thesis. The Drude model which I provided in section 3.2 is used for the center layer material. All the required parameters also have been provided in section 3.2. I have carried out a detailed mode analysis using COMSOL Multiphysics to investigate the effects of different

parameters on the model properties. In general, the implementation of the model has the following steps:

1. Create geometric object
2. Set up the global definition and component definitions
3. Define the electric and magnetic interfaces
4. Specify materials properties
5. Create the mesh and run the simulation
6. Receive the result

The geometric object (with mesh) can be modelled as Fig. 3.5a and the partial enlarged drawing of the center part can be seen in Fig. 3.5b.

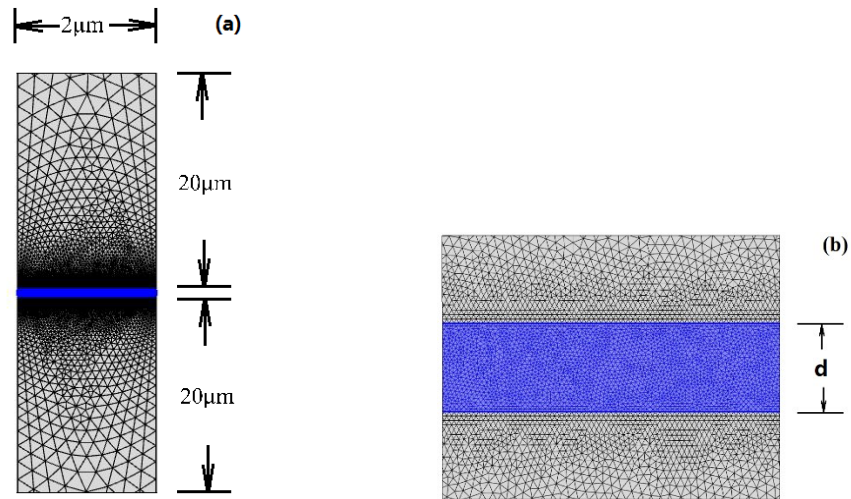


Figure 3.5 2D dimensional drawing (a) outside view with mesh (not scaled) and (b) partial enlarged drawing of the center part

This dimension ensured the energy density and the intensity fields are entirely confined in this geometric object model. In addition, to obtain accurate results in the simulation, the maximum mesh size has been set at 5 nm.

3.6 SIMULATION WITH DIFFERENT CORE THICKNESSES AROUND TC FREQUENCY AT 40 KELVINS

As I discussed in Section 3.4, the thickness d of the central layer plays a significant role in the properties on the ISCI waveguide. Therefore, the first simulation was to numerically analyze the properties of the ISCI waveguide versus the parameter of d around the TC frequency at the operating temperature of 40K. The function of energy density has been integrated in COMSOL Multiphysics. For mode analysis, the effective mode index also can be computed by the software. Note that more than one mode exists, but as I discussed in section 3.4, in this thesis, I am only interested in the fundamental SM.

To start with an example, I set the thickness d equal to 100 nm and the wavelength equal to 1550 nm. The cladding insulator is assumed as air ($\epsilon_I = 1$). After simulation, the normalized energy density plot has been created by COMSOL Multiphysics. To see the plot clearly, a partial enlarged drawing of the normalized energy density plot in the center part has been provided in Fig 3.6.

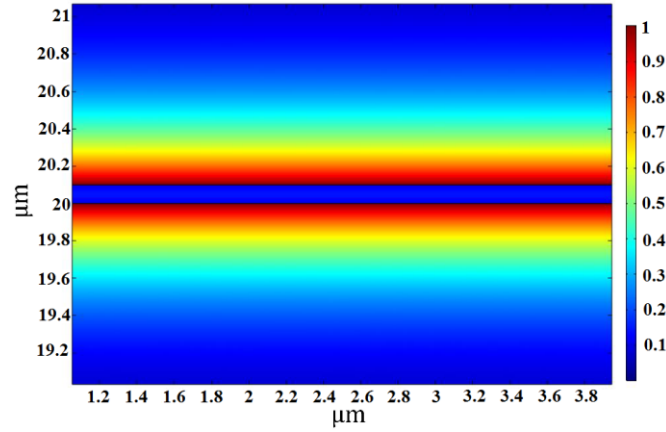


Figure 3.6 a partial enlarged drawing of the normalized energy density plot in the center part

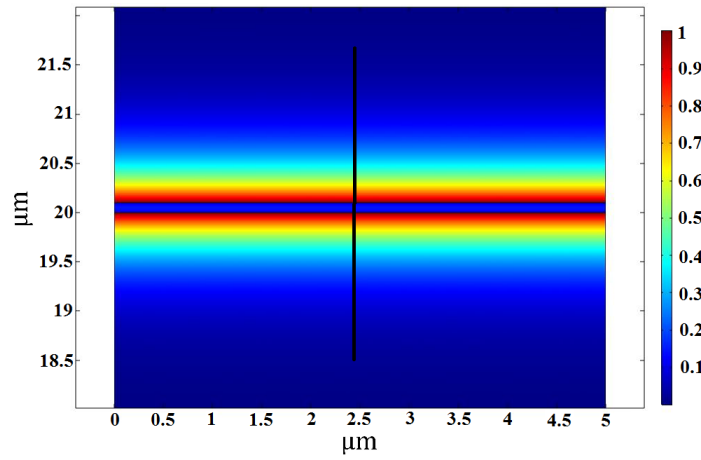


Figure 3.7 a vertical cut line at the center (line is not scaled)

It is clear that the energy density spreads out from the surface of the SC core. The closer to the interface of the core and cladding, the higher the energy density. I can also draw a vertical cut line at the center, which can be seen in Fig. 3.7. Then I can receive a 1D line plot of the normalized energy density in Fig. 3.8. Now I can quantitatively evaluate the energy density throughout the entire center line. I can receive the same result as shown in Fig. 3.6; however, a small amount of energy exists in the SC core, which I cannot see from Fig. 3.6. This

phenomenon happens due to the interaction between the SPPs at the two metal surfaces, giving rise to the coupled mode.

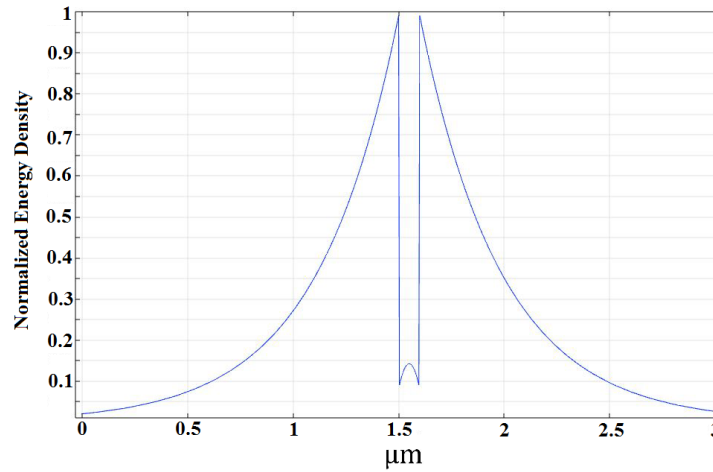


Figure 3.8 1D line plot of the normalized energy density

Now I can set up the core thickness starting from 90 nm, increasing in 10 nm increments, to 200 nm. Three wavelengths were chosen, namely 1500 nm, 1550 nm and 1600 nm.

After simulation, the following tables with the simulation result can be seen in Table 3.2(a), 3.2(b) and 3.2(c).

Table 3.2 (a) The mode size and the propagation length at wavelength 1500 nm

Core thickness (nm)	Effective mode index of the fundamental mode	L_m (μm)	L_p (m)	L_{Np}	L_{Nm}
90	1.0482+2.7908E-6i	0.7678	0.0442	29464.6618	1.0237
100	1.0595+3.5870E-6i	0.6902	0.0344	22924.3015	0.9202
110	1.0718+4.4850E-6i	0.6262	0.0275	18334.2419	0.8349
120	1.0852+5.5259E-6i	0.5722	0.0223	14880.7539	0.7630
130	1.0997+6.7245E-6i	0.5260	0.0183	12228.2942	0.7014
140	1.1151+8.0964E-6i	0.4859	0.0152	10156.3374	0.6478
150	1.1316+9.6570E-6i	0.4505	0.0128	8515.0358	0.6007
160	1.1490+1.1421E-5i	0.4190	0.0108	7199.6294	0.5587
170	1.1673+1.3403E-5i	0.3908	0.0092	6135.0600	0.5211
180	1.1864+1.5614E-5i	0.3653	0.0079	5266.3899	0.4870
190	1.2061+1.8062E-5i	0.3421	0.0068	4552.6483	0.4561
200	1.2265+2.0750E-5i	0.3209	0.0059	3962.7708	0.4279

Table 3.2 (b) The mode size and the propagation length at wavelength 1550 nm

Core thickness (nm)	Effective mode index of the fundamental mode	L_m (μm)	L_p (m)	L_{Np}	L_{Nm}
90	1.0408+1.9904E-6i	0.8690	0.0620	39980.0618	1.1214
100	1.0501+2.7463E-6i	0.7835	0.0449	28975.8693	1.0109
110	1.0603+3.4094E-6i	0.7132	0.0362	23340.0035	0.9202
120	1.0713+4.1677E-6i	0.6542	0.0296	19093.6580	0.8442
130	1.0831+5.0281E-6i	0.6040	0.0245	15826.4046	0.7794
140	1.0956+5.9974E-6i	0.5606	0.0206	13268.5483	0.7234
150	1.1089+7.0818E-6i	0.5226	0.0174	11236.8714	0.6743
160	1.1227+8.2864E-6i	0.4890	0.0149	9603.3209	0.6309
170	1.1371+9.6152E-6i	0.4590	0.0128	8276.1825	0.5922
180	1.1520+1.1070E-5i	0.4320	0.0111	7188.3575	0.5574
190	1.1673+1.2651E-5i	0.4076	0.0097	6289.8337	0.5260
200	1.1830+1.4357E-5i	0.3855	0.0086	5542.7182	0.4974

Table 3.2 (c) The mode size and the propagation length at wavelength 1600 nm

Core thickness (nm)	Effective mode index of the fundamental mode	L_m (μm)	L_p (m)	L_{Np}	L_{Nm}
90	1.0357+1.7673E-6i	0.9594	0.0698	43619.7406	1.1992
100	1.0438+2.2310E-6i	0.8664	0.0553	34553.7683	1.0830
110	1.0526+2.7581E-6i	0.7902	0.0447	27950.3667	0.9878
120	1.0620+3.3560E-6i	0.7266	0.0368	22970.7804	0.9082
130	1.0721+4.0287E-6i	0.6725	0.0306	19135.2270	0.8407
140	1.0828+4.7797E-6i	0.6260	0.0258	16128.4743	0.7824
150	1.0941+5.6121E-6i	0.5853	0.0220	13736.4015	0.7317
160	1.1058+6.5279E-6i	0.5496	0.0189	11809.3865	0.6870
170	1.1179+7.5281E-6i	0.5178	0.0164	10240.2927	0.6472
180	1.1303+8.6127E-6i	0.4893	0.0143	8950.7624	0.6116
190	1.1431+9.7800E-6i	0.4636	0.0126	7882.4121	0.5795
200	1.1560+ 1.1027E-5i	0.4403	0.0112	6991.0257	0.5504

Once I have all the data from Tables 3.2(a), (b) and (c), I can draw Fig. 3.9 (a) and (b) to show the results. The results show that the mode size decreases as the thickness of SC core d increases, which indicates that the localization of the plasmonic waveguide mode becomes tighter, or in other words, more energy will be distributed in the vicinity of SC surface for the thicker SC

core, giving rise to the shorter propagation length, which is reasonably shown in Fig. 3.9 (a) and (b); i.e. the propagation length decreases with increasing d . From Fig. 3.9 (b), I can also see that the diffraction limit cannot be overcome when the value of d is smaller than a certain value. For example, when the wavelength is 1550 nm, the minimal thickness of the SC core should be greater than 100 nm to surpass the diffraction limit. Furthermore, it is noted that both L_{Nm} and L_{Np} decrease as frequency increases. This is because that at a high frequency, the larger values of real and imaginary parts of permittivity lead to a smaller penetration depth and higher propagation loss, respectively, thus resulting in a smaller mode size and propagation length.

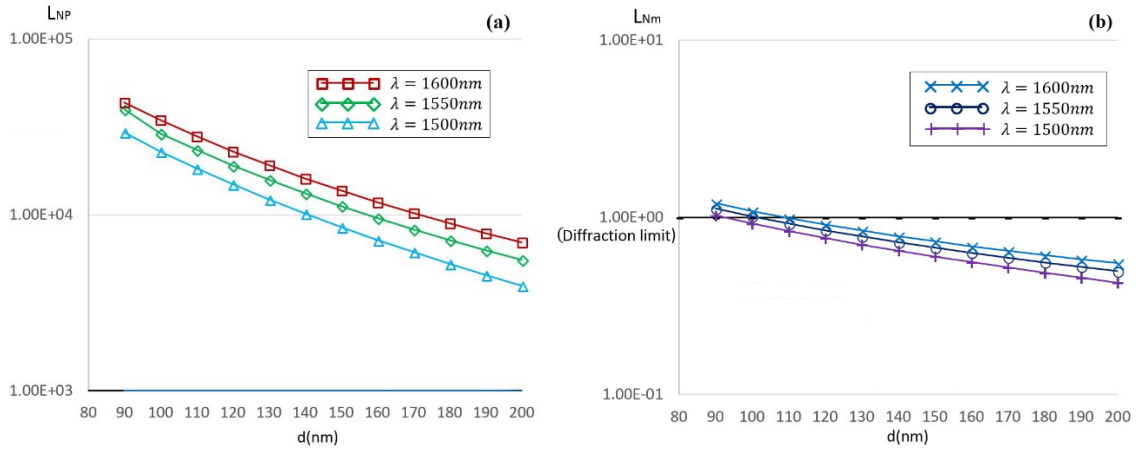


Figure 3.9 (a) Normalized propagation length and (b) Normalized mode size of ISCI waveguide as a function of SC core thickness d around TC frequencies

3.7 SIMULATION WITH DIFFERENT OPERATING TEMPERATURES AND PERMITTIVITY WITH FIXED CORE THICKNESS

Another reality is that the permittivity of SC is highly dependent on the operating temperature, as illustrated in Equation 3.3, indicating that the mode properties of the ISCI waveguide are also influenced by the operating temperature. Therefore, it is important to investigate the relationship between mode properties and operating temperature. In order to achieve subwavelength mode localization, the thickness of the superconductor core was chosen as 110 nm at wavelength 1550 nm. The operating temperature was chosen as 20 K to 80 K, increasing by 20K each time and the permittivity ϵ_1 was chosen as 1.0 to 1.6, increasing by 0.1 incrementally. By simulation, I can achieve the data from COMSOL Multiphysics, which is shown in Table 3.3.

Table 3.3 The mode size and the propagation length at fixed wavelength and core thickness at different temperature and relative permittivity

Relative permittivity	Temperature (K)	Effective mode index of the fundamental mode	L_m (μm)	L_p (m)	L_{Np}	L_{Nm}
1.0	20	1.0603+6.1034E-8i	0.7132	2.021	1.304E+6	0.9202
1.0	40	1.0603+3.4094E-6i	0.7132	3.618E-2	2.334E+4	0.9202
1.0	60	1.0603+4.6441E-5i	0.7132	2.656E-3	1.714E+3	0.9202
1.0	80	1.0603+5.1370E-4i	0.7132	2.401E-4	1.549E+2	0.9202
1.1	20	1.1964+1.1615E-7i	0.5283	1.062	6.851E+5	0.6816

Relative permittivity	Temperature (K)	Effective mode index of the fundamental mode	L_m (μm)	L_p (m)	L_{Np}	L_{Nm}
1.1	40	1.1964+6.4887E-6i	0.5283	1.901E-2	1.226E+4	0.6816
1.1	60	1.1964+8.8385E-5i	0.5283	1.396E-3	9.004E+2	0.6816
1.1	80	1.1964+9.7764E-4i	0.5283	1.262E-4	8.140E+1	0.6816
1.2	20	1.3544+2.2606E-7i	0.3863	5.456E-1	3.520E+5	0.4984
1.2	40	1.3544+1.2628E-5i	0.3863	9.767E-3	6.302E+3	0.4984
1.2	60	1.3544+1.7201E-4i	0.3863	7.171E-4	4.626E+2	0.4984
1.2	80	1.3543+1.9026E-3i	0.3863	6.483E-5	4.183E+1	0.4984
1.3	20	1.5530+4.7694E-7i	0.2705	2.586E-1	1.668E+5	0.3490
1.3	40	1.5530+2.6643E-5i	0.2705	4.630E-3	2.987E+3	0.3490
1.3	60	1.5530+3.6291E-4i	0.2708	3.399E-4	2.193E+2	0.3494
1.3	80	1.5530+4.0138E-3i	0.2715	3.073E-5	1.983E+1	0.3503
1.4	20	1.8493+1.2996E-6i	0.1711	9.490E-2	6.123E+4	0.2207
1.4	40	1.8493+7.2602E-5i	0.1711	1.699E-3	1.096E+3	0.2207
1.4	60	1.8493+9.8894E-4i	0.1711	1.247E-4	8.047E+1	0.2207
1.4	80	1.8490+1.0932E-2i	0.1711	1.128E-5	7.279	0.2208
1.5	20	2.6385+0.4922i	0.0610	2.506E-7	1.617E-1	0.0787
1.5	40	2.6381+0.4920i	0.0610	2.507E-7	1.617E-1	0.0787

Relative permittivity	Temperature (K)	Effective mode index of the fundamental mode	L_m (μm)	L_p (m)	L_{Np}	L_{Nm}
1.5	60	2.6324+0.4891i	0.0614	2.522E-7	1.627E-1	0.0792
1.5	80	2.5710+0.4634i	0.0660	2.662E-7	1.717E-1	0.0851
1.6	20	2.2466+1.111284i	0.0843	1.110E-7	7.161E-2	0.1088
1.6	40	2.2465+1.111122i	0.0843	1.110E-7	7.162E-2	0.1088
1.6	60	2.2457+1.109056i	0.0845	1.112E-7	7.175E-2	0.1090
1.6	80	2.2365+1.086999i	0.0859	1.135E-7	7.321E-2	0.1109

Once I have all the data from Table 3.3, I can draw Fig. 3.10 to show the results.

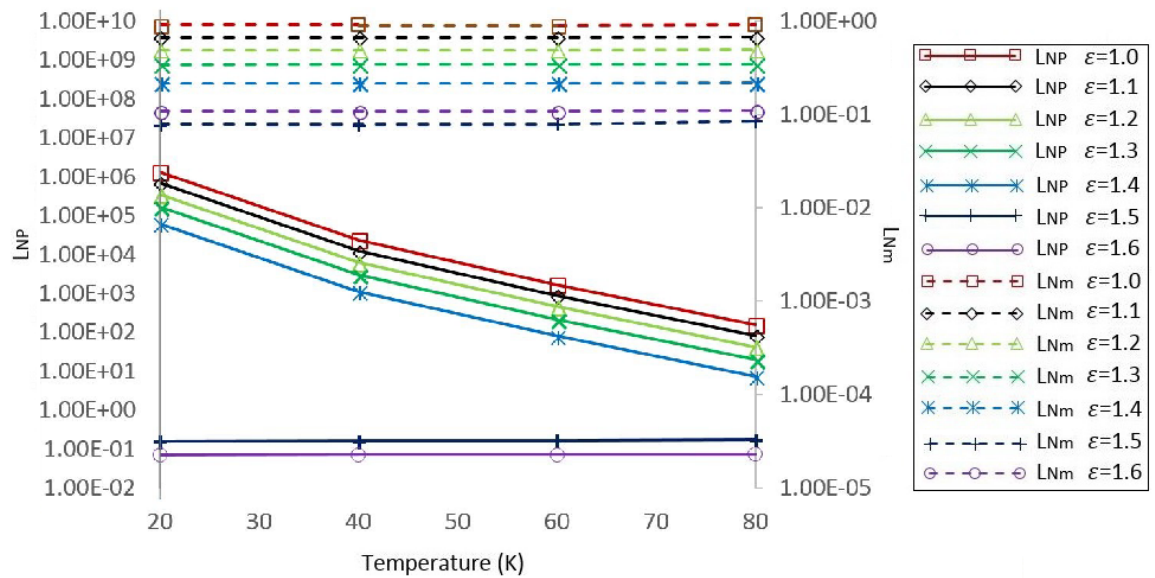


Figure 3.10 Mode characteristics of ISCI waveguides as a function of temperature and ϵ_1 at TC

frequency with thickness of superconductor core of $d=110$ nm

Fig. 3.10 shows that L_{Np} decreases with increasing temperature due to the increasing losses. Moreover, the L_{Np} decreases when ϵ_I increases. This can be explained by the theory of boundary continuities. The normal components of electric displacement at the boundary are the same all the time, i.e., $\epsilon_I E_{I\perp} = \epsilon_{sc} E_{sc\perp}$. A reduced L_{Np} results from the decreasing of the electric field in the insulator with increasing ϵ_I . Furthermore, it is found that the temperature has a very small impact on L_{Nm} . For example, the value of L_{Nm} is almost the same from 20 K to 80 K for a fixed ϵ_I . For a smaller value of ϵ_I , the enhanced field in the insulator causes the decreased penetration depth into YBCO. Therefore, L_{Nm} decreases with increasing ϵ_I .

3.8 SIMULATION WITH DIFFERENT MATERIAL

To quantitatively validate the advantages of the proposed ISCI waveguide, the SC core for the ISCI waveguide and IMI waveguides with $\epsilon_I = 1.0$ and $T = 40$ K will be simulated. In addition, a conventional SC material, niobium (N_b), was added as the matched group to illustrate the superiority of unconventional SC YBCO. The parameters of the Drude model for N_b are fixed as $T_c = 9.26$ K, $N = 9.4 \times 10^{27} \text{ m}^{-3}$, and $\tau = 7.3 \times 10^{-10} \text{ s}$ [26]. By simulation, I can achieve the data from COMSOL Multiphysics, which is shown in Table 3.4(a), (b) and (c).

Table 3.4 (a) Normalized propagation length and normalized mode size of ISCI with material YBCO

Core thickness (nm)	Effective mode index of the fundamental mode	L_m (μm)	L_p (μm)	L_{Np}	L_{Nm}
100	1.0501+2.7463E-6i	0.7835	44912.5974	2.8976E+10	1.0109
110	1.0603+3.4094E-6i	0.7132	36177.0054	2.3340E+10	0.9202
120	1.0713+4.1677E-6i	0.6542	29595.1698	1.9094E+10	0.8442
130	1.0831+5.0281E-6i	0.6040	24530.9272	1.5826E+10	0.7794
140	1.0956+5.9974E-6i	0.5606	20566.2499	1.3269E+10	0.7234
150	1.1089+7.0818E-6i	0.5226	17417.1507	1.1237E+10	0.6743
160	1.1227+8.2864E-6i	0.4890	14885.1474	9.6033E+9	0.6309
170	1.1371+9.6152E-6i	0.4590	12828.0829	8.2761E+9	0.5922
180	1.1520+1.1070E-5i	0.4320	11141.9541	7.1883E+9	0.5574
190	1.1673+1.2651E-5i	0.4076	9749.2422	6.2898E+9	0.5260
200	1.1830+1.4357E-5i	0.3855	8591.2132	5.5427E+9	0.4974

Table 3.4 (b) Normalized propagation length and normalized mode size of ISCI with material N_b

Core thickness (nm)	Effective mode index of the fundamental mode	L_m (μm)	L_p (μm)	L_{Np}	L_{Nm}
100	1.0141+2.7348E-6i	1.4800	45101.2472	2.9098E+10	1.9097
110	1.0158+3.3845E-6i	1.4006	36444.1045	2.3512E+10	1.8072
120	1.0173+4.0555E-6i	1.3376	30414.1510	1.9622E+10	1.7259
130	1.0186+4.7291E-6i	1.2870	26081.9902	1.6827E+10	1.6607
140	1.0198+5.3892E-6i	1.2461	22887.3002	1.4766E+10	1.6079
150	1.0209+6.0230E-6i	1.2127	20478.9011	1.3212E+10	1.5648
160	1.0218+6.6211E-6i	1.1853	18629.0572	1.2019E+10	1.5294
170	1.0226+7.1772E-6i	1.1627	17185.5603	1.1087E+10	1.5002
180	1.0233+7.6879E-6i	1.1440	16043.9145	1.0351E+10	1.4761
190	1.0239+8.1520E-6i	1.1285	15130.6369	9.7617E+9	1.4561
200	1.0244+8.5698E-6i	1.1155	14392.9284	9.2858E+9	1.4394

Table 3.4 (c) Normalized propagation length and normalized mode size of IMI with material A_g

Core thickness (nm)	Effective mode index of the fundamental mode	L_m (μm)	L_p (μm)	L_{Np}	L_{Nm}
100	1.0038+8.0962E-5i	2.8217	1523.4836	9.8289E+8	3.6408
110	1.0038+8.4802E-5i	2.7994	1454.4986	9.3839E+8	3.6122
120	1.0039+8.7488E-5i	2.7854	1409.8381	9.0957E+8	3.5941
130	1.0039+8.9342E-5i	2.7764	1380.5804	8.9070E+8	3.5825
140	1.0039+9.0610E-5i	2.7708	1361.2717	8.7824E+8	3.5753
150	1.0039+9.1469E-5i	2.7672	1348.4776	8.6999E+8	3.5706
160	1.0039+9.2049E-5i	2.7650	1339.9826	8.6450E+8	3.5677
170	1.0039+9.2439E-5i	2.7635	1334.3382	8.6086E+8	3.5658
180	1.0039+9.2699E-5i	2.7626	1330.5897	8.5844E+8	3.5647
190	1.0039+9.2873E-5i	2.7620	1328.1000	8.5684E+8	3.5639
200	1.0039+9.2988E-5i	2.7616	1326.4500	8.5577E+8	3.5634

Once I have all the data from Table 3.4(a), (b) and(c), I can draw Fig. 3.11(a) and (b) to show the results.

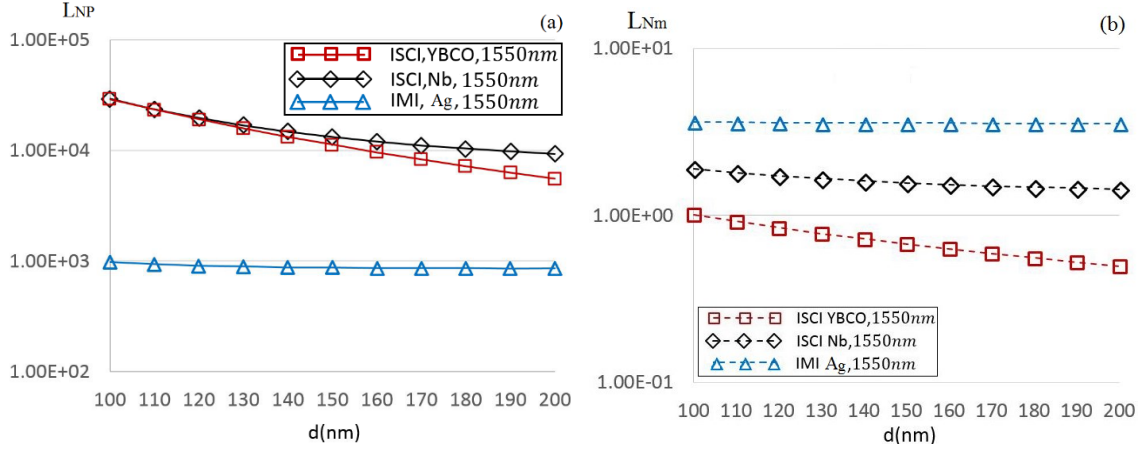


Figure 3.11 (a) Normalized propagation length and (b) normalized mode size of ISCI (N_b and YBCO) and IMI waveguides

From Fig. 3.11 (a), it is clear that the normalized propagation lengths of the SC-based plasmonic waveguide are similar and much larger than that of Ag-based SPPs waveguide. For example, from Table 3.4 (a), (b) and (c), with parameters of $d = 110$ nm and $\lambda = 1550$ nm, the propagation length for the YBCO- and N_b -based SPPs waveguides are around 36 mm, which is at least 20-fold extended than that of the Ag-based waveguide, which is 1.5 mm. The results illustrate that the SC-based plasmonic waveguide has a superior capability for low-loss optical guiding. Moreover, from Fig. 3.11 (a), I find that the conventional SC-based waveguide has an even longer normalized propagation length compared to the unconventional SC-based waveguide when the thickness increases. However, this relatively long normalized propagation length is attained by sacrificing the mode size, as shown in Fig. 3.11 (b). In this case, the normalized mode size of unconventional SC-based waveguide is much smaller than those for the other two waveguides. What is important is that only the YBCO-based SPPs waveguide can break the diffraction limit when the thickness is larger than 100 nm. For instance, with parameters of $d = 110$ nm and $\lambda =$

1550 nm, the mode size for the IMI waveguide is increased more than three-fold compared to the YBCO-based waveguide (i.e. $L_m = 713$ nm for the YBCO-based waveguide and $L_m = 2799$ nm for the IMI A_g waveguide). The mode size for the N_b -based SPPs waveguide is increased two-fold compared to that of the YBCO-based waveguide (i.e. $L_m = 1400$ nm for the N_b -based waveguide). Notice that the minimal mode size should be less than half of the wavelength, which is 775 nm, to overcome diffraction limit. Therefore, the results shown in Fig. 3.11 (b) reveal that only the YBCO-based waveguide has the capacity to localize the waveguide mode beyond the diffraction limit.

3.9 FIGURE OF MERIT (FoM) FOR SC-BASED AND IMI WAVEGUIDES

The FoM is defined as $\frac{L_{NP}}{L_{Nm}}$. For plasmonic waveguides, it is known that there is a trade-off between the mode size and propagation length; in other words, the realization of small mode size is at the price of shorter propagation length, and vice versa. Therefore, from the definition of FoM, it is noted that the larger the value of FoM, the better performance the waveguide possesses. The mode size and the propagation length have been calculated by COMSOL Multiphysics. Therefore, the FoM can be calculated, too. Table 3.5 (a), (b) and (c) show the FoM for SC-based (i.e. YBCO and N_b) and IMI waveguides with different core thickness and fixed permittivity ($\epsilon_l = 1$) and temperature 40K at TC frequency.

Table 3.5 (a) FoMs for YBCO -based waveguides

Core thickness (nm)	Effective mode index of the fundamental mode	L_{np}	L_{nm}	FoM
100	1.0501+2.7463E-6i	28975869302	1.010932219	28662524320
110	1.0603+3.4094E-6i	23340003478	0.920212089	25363721848
120	1.0713+4.1677E-6i	19093657966	0.844180054	22617992304
130	1.0831+5.0281E-6i	15826404635	0.779378055	20306454013
140	1.0956+5.9974E-6i	13268548346	0.723350773	18343172968
150	1.1089+7.0818E-6i	11236871442	0.674313	16664177389
160	1.1227+8.2864E-6i	9603320934	0.630941476	15220620773
170	1.1371+9.6152E-6i	8276182531	0.592239513	13974384263
180	1.1520+1.1070E-5i	7188357506	0.557445837	12895167626
190	1.1673+1.2651E-5i	6289833677	0.525972002	11958495225
200	1.1830+1.4357E-5i	5542718188	0.497358615	11144309208

Table 3.5 (b) FoMs for N_b -based waveguides

Core thickness (nm)	Effective mode index of the fundamental mode	L_{np}	L_{nm}	FoM
100	1.0141+2.7348E-6i	29097578860	1.909664386	15237011841
110	1.0158+3.3845E-6i	23512325485	1.807198546	13010372066
120	1.0173+4.0555E-6i	19622032901	1.725921067	11369021028
130	1.0186+4.7291E-6i	16827090474	1.660694263	10132563741
140	1.0198+5.3892E-6i	14766000139	1.607863928	9183613043
150	1.0209+6.0230E-6i	13212194258	1.564760253	8443590147
160	1.0218+6.6211E-6i	12018746570	1.529387602	7858535373
170	1.0226+7.1772E-6i	11087458261	1.500225369	7390528444
180	1.0233+7.6879E-6i	10350912578	1.476094664	7012363660
190	1.0239+8.1520E-6i	9761701198	1.456069101	6704146931
200	1.0244+8.5698E-6i	9285760287	1.439411533	6451080927

Table 3.5 (c) FoMs for IMI waveguides

Core thickness (nm)	Effective mode index of the fundamental mode	L_{np}	L_{nm}	FoM
100	1.0038+8.0962E-5i	982892657.8	3.64084991	269962421.4
110	1.0038+8.4802E-5i	938386180.3	3.612186975	259783390.7
120	1.0039+8.7488E-5i	909572948.3	3.594058574	253076829.3
130	1.0039+8.9342E-5i	890697029.3	3.582502966	248624226.6
140	1.0039+9.0610E-5i	878239777	3.575276635	245642468.1
150	1.0039+9.1469E-5i	869985577.7	3.570643767	243649502.5
160	1.0039+9.2049E-5i	864504874.3	3.567699807	242314354
170	1.0039+9.2439E-5i	860863336.1	3.565827855	241420329.6
180	1.0039+9.2699E-5i	858444991.5	3.564693704	240818724.6
190	1.0039+9.2873E-5i	856838723.4	3.563876967	240423205.2
200	1.0039+9.2988E-5i	855774180.8	3.56339622	240156897.5

Once I have all the data from Table 3.5(a), (b) and(c), I can draw Fig. 3.12 to show the results. From Fig. 3.12, it is obvious that the FoMs for the ISCI waveguides are always higher than that of the IMI waveguide. In addition, the FoMs for the YBCO-based waveguides are always higher than that of the N_b -based waveguides. For example, The FoM for the

YBCO-based waveguide is at least 97-fold improved with parameters of $d = 110 \text{ nm}$ and $\lambda = 1550 \text{ nm}$ compared to IMI waveguide. Likewise, The FoM for the YBCO-based waveguide is about 2-fold improved with parameters of $d = 110 \text{ nm}$ and $\lambda = 1550 \text{ nm}$ compared to N_b -based waveguides. From the above, I can see that the YBCO-based waveguides have the best performance among those three waveguides.

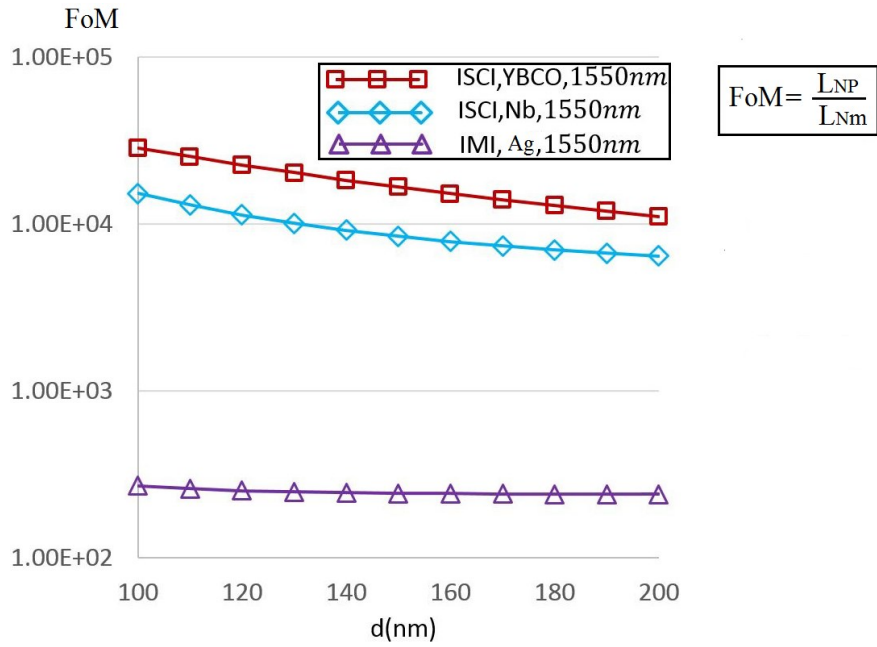


Figure 3.12 FoMs for SC-based (i.e. YBCO and N_b) and IMI waveguides

CHAPTER 4 CONCLUSION AND FUTURE WORK

4.1 CONCLUSIONS FROM THE RESEARCH AND DISCUSSIONS

In the thesis, I have proposed a novel SC-based symmetric plasmonic waveguide. This waveguide contains a YBCO SC core and a dielectric cladding. The investigation of the SPPs mode properties around TC frequency has been performed. By using the COMSOL Multiphysics simulation software, this proposed structure has been simulated with various parameters, namely the working frequency, the core thickness, the cladding permittivity and the working temperature. In addition, this proposed YBCO SC waveguide has been compared with a metal (Ag) and conventional SC (N_b) core waveguide. The quantitative evaluation of SPPs waveguide mode characteristics focused on two key parameters, namely the propagation length (L_p) and the mode size (L_m). I found that the propagation length of the YBCO ISCI waveguide can be extended up to 36000 μm with a mode size as small as $\lambda/4$ at the TC frequency range. The results illustrate that the proposed YBCO-based plasmonic waveguide allows the SPPs transport on the subwavelength scale beyond the diffraction limit as well as with a long propagation length. Furthermore, the results show that the unconventional SC-based waveguide possesses better properties than other conventional materials. The outstanding properties would offer a novel approach to design new integrated plasmonic circuits and biosensors.

In this thesis, I heavily relied on COMSOL Multiphysics to solve ISCI waveguide simulation

problems with the finite element analysis method. Although this commercial software has been well developed and used by many researchers successfully, there are some black boxes due to intellectual property. Some integrated functions do not provide the source code. Therefore, even if there are some kinds of bugs, they would be difficult to find. To eliminate the negative impact, I have repeated all the simulation in Ref. 23 by using COMSOL Multiphysics at TC frequency. To the end, it turns out that all the results are exactly the same as the author obtained. This repeated work provides me confidence to accept COMSOL Multiphysics as my working tools. However, I may think about the use of some other software to simulate the same problem. Hence, the result can be validated by comparing the outputs coming from different software.

I use YBCO as the SC core for the ISCI waveguide. Although the YBCO is a high-temperature superconductor, the critical temperature is still very low. The operating temperature could be a disadvantage. For example, it would be hard to use it in a portable device because the device needs a constant cooling system to keep the YBCO under the critical temperature.

The trade-off between the mode propagation length with low loss and mode confinement still exists. Namely, a long propagation length will lead to a large mode size and vice versa. From the results I received from this thesis, the ISCI structure may be appropriate for some applications, but not universally. There needs to be more research to have a well-balanced model.

4.2 FUTURE WORK

As said in section 4.1, one possible method to validate these simulation results is to use some other software to simulate the same model. With the comparison, the accuracy of the various details in this model can be authenticated.

Graphene is another good alternative plasmonic material owing to its zero band-gap and high carrier mobility. It is possible to simulate the model with graphene core layer and find the guiding properties of the waveguide. In addition, the comparison can be made between the SC core and the graphene core model.

Also, all the results I received are based on the simulation. Practically, I need to find a way to build the physical model which integrates three layers as well as to make the model superconduct and test the results with the simulated data.

BIBLIOGRAPHY

- [1] Gao, Yongkang, et al. "Plasmonic interferometers for label-free multiplexed sensing." *Optics express* 21.5 (2013): 5859-5871
- [2] Oulton, Rupert F., et al. "Plasmon lasers at deep subwavelength scale." *Nature* 461.7264 (2009): 629.
- [3] Lin, Pin-Tso, et al. "Trapping particles using waveguide-coupled gold bowtie plasmonic tweezers." *Lab on a Chip* 14.24 (2014): 4647-4652.
- [4] Ma, Youqiao, et al. "A hybrid wedge-to-wedge plasmonic waveguide with low loss propagation and ultra-deep-nanoscale mode confinement." *Journal of Lightwave Technology* 33.18 (2015): 3827-3835.
- [5] Maier, Stefan Alexander. Plasmonics: fundamentals and applications. *Springer Science & Business Media*, 2007.
- [6] Zheludev, Nikolay I., et al. "Lasing spaser." *Nature Photonics* 2.6 (2008): 351.
- [7] Maier, Stefan A., et al. "Local detection of electromagnetic energy transport below the diffraction limit in metal nanoparticle plasmon waveguides." *Nature materials* 2.4 (2003): 229.
- [8] Pile, David FP, et al. "Theoretical and experimental investigation of strongly localized plasmons on triangular metal wedges for subwavelength waveguiding." *Applied Physics Letters* 87.6 (2005): 061106.

- [9] Yang, Xiaodong, et al. "Optical forces in hybrid plasmonic waveguides." *nano Letters* 11.2 (2011): 321-328.
- [10] Eldlio, Mohamed, et al. "A THz semiconductor hybrid plasmonic waveguide with fabrication-error tolerance." *Japanese Journal of Applied Physics* 56.1 (2016): 010306.
- [11] Holmgaard, Tobias, Jacek Gosciniak, and Sergey I. Bozhevolnyi. "Long-range dielectric-loaded surface plasmon-polariton waveguides." *Optics express* 18.22 (2010): 23009-23015.
- [12] McPeak, Kevin M., et al. "Plasmonic films can easily be better: rules and recipes." *ACS photonics* 2.3 (2015): 326-333.
- [13] Ma, Youqiao, et al. "Hybrid nanowedge plasmonic waveguide for low loss propagation with ultra-deep-subwavelength mode confinement." *Optics letters* 39.4 (2014): 973-976.
- [14] West, Paul R., et al. "Searching for better plasmonic materials." *Laser & Photonics Reviews* 4.6 (2010): 795-808.
- [15] Berini, Pierre. "Long-range surface plasmon polaritons." *Advances in optics and photonics* 1.3 (2009): 484-588.
- [16] Smith, D. Y., et al. "Handbook of optical constants of solids." *Handbook of Optical Constants of Solids I* (1985): 369-406.

- [17] Mao, Xiaou, and Michael Cada. "Optical Surface Plasmon in Semiconductors." Integrated Photonics Research, Silicon and Nanophotonics. *Optical Society of America*, 2013.
- [18] Ashcroft, Neil W., and N. David Mermin. "Solid state physics (Saunders college, Philadelphia, 1976)." *Google Scholar* (2010): 461.
- [19] Raether, Heinz. "Surface plasmons on smooth surfaces." Surface plasmons on smooth and rough surfaces and on gratings. *Springer, Berlin, Heidelberg*, 1988. 4-39.
- [20] Novotny, Lukas, and Bert Hecht. Principles of nano-optics. *Ambridge university press*, 2012.
- [21] Ma, Youqiao, et al. "Semiconductor-based plasmonic interferometers for ultrasensitive sensing in a terahertz regime." *Optics letters* 42.12 (2017): 2338-2341.
- [22] Majedi, A. Hamed. "Theoretical investigations on THz and optical superconductive surface plasmon interface." *IEEE Transactions on Applied Superconductivity* 19.3 (2009): 907-910.
- [23] Ma, Youqiao, et al. "Plasmonic properties of superconductor–insulator–superconductor waveguide." *Applied Physics Express* 9.7 (2016): 072201.
- [24] Tsiatmas, Anagnostis, et al. "Superconducting plasmonics and extraordinary transmission." *Applied Physics Letters* 97.11 (2010): 111106.

- [25] Chen, Yang, et al. "High-efficiency apodized-imaging chip-fiber grating coupler for silicon nitride waveguides." *Optics letters* 41.21 (2016): 5059-5062.
- [26] Mei, Kenneth K., and G-C. Liang. "Electromagnetics of superconductors." *IEEE transactions on microwave theory and techniques* 39.9 (1991): 1545-1552.